DC-Biased Sinusoidal Current Excited Switched Reluctance Motor Drives Based on Flux Modulation Principle

Zhiyue Yu, *Student Member, IEEE*, Chun Gan, *Member, IEEE*, Yu Chen, *Student Member, IEEE*, and Ronghai Qu, *Fellow, IEEE*

***Abstract*—This article proposes a novel current control technique for three-phase switched reluctance motor (SRM) drives with harmonic current suppression, based on developed flux modulation principle. For conventional SRM control systems, the unsmooth and discontinuous stator current cause serious torque ripple, vibration, and noise, due to the doubly salient motor structure. In order to overcome shortcomings in conventional drives, the developed flux modulation principle is employed for the SRM in this article, where the working principle is investigated in detail, including the excitation magnetic field, flux modulator, and armature magnetic field. Then, a new control strategy is presented to generate the dc-biased sinusoidal current, by employing the modular open-winding converter. Furthermore, a harmonic current suppression strategy is put forward for the new drive to improve the motor performance, by employing a developed vector proportional integral control scheme. Compared to existing SRM drives, the torque ripple and motor vibration can be both significantly reduced, the motor structure and winding arrangement do not need to be changed, and the robustness of the motor system is improved. Finally, experiments are carried out on a three-phase 12/8 SRM prototype to verify the effectiveness of the proposed SRM drive and control strategy.**

***Index Terms*—Flux modulation, harmonic current suppression, open-winding converter, switched reluctance motor (SRM), torque ripple, vibration.**

I. Introduction

DUE to advantages of simple doubly salient structure, high starting torque, rare-earth free, low cost, and good speed control performance, switched reluctance motors (SRMs) have received much attention in various applications [1]–[4]. With the rare-earth sources becoming increasingly rare, SRMs are considered to be a promising solution for applications in electric vehicles [5]–[9], household appliances [10], automotive traction [11], [12], and aircraft starters and generators [13]–[15]. In terms of the control strategy, the current chopping control (CCC) method is usually adopted in the SRM drive, due to advantages of simple calculation and flexible control ability [16], [17], and the stator current waveform is approximate to the discontinuous square waveform. However, the double salient structure and the abundant high-order harmonic components in the phase current will generate large torque ripple, vibration, and noise, which limit the SRMs for industrial applications [18].

For SRMs, the electromagnetic force can be decomposed into the radial electromagnetic force and tangential electromagnetic force. The radial force is the source of the vibration and noise, and the tangential force provides the output torque. However, the rapid change in tangential force will cause torque ripple. Hence, to suppress the torque ripple and vibration, both the radial and tangential force should be considered comprehensively. There have been several investigations on torque ripple reduction and vibration minimization. In terms of the motor topology, several shape redesign methods of the stator and rotor teeth are proposed in [19]–[22] to eliminate the torque ripple. In [23], the step airgap and cambered rotor teeth are adopted for torque ripple reduction. A vibration reduction strategy is put forward in [24] by inserting insulating nonmagnetic ceramic gaskets between the stator teeth. In [25], the stator and rotor skewing method is adopted to reduce vibration and noise in SRM drives.

In terms of motor control strategies, several advanced control schemes have been investigated. In [26], an active vibration reduction method is proposed. By inserting a short zero-voltage loop into the current commutation region, the vibration caused by the sudden current change can be reduced. Besides, a hybrid excitation strategy is proposed in [27], where the vibration and noise can be reduced since the changing rate of the excitation voltage and magnetic flux during the current commutation region is decreased. In [28], the independent winding structure is employed. By independently controlling the winding current, a required radial force can be generated on the rotor to counteract the vibration.

For torque ripple reduction, referring to the induction motor control method, the direct torque control (DTC) scheme is developed in SRM drives [18], [29]–[31]. The voltage vector of the power converter is selected by comparing the reference and actual value of the torque and magnetic flux amplitude. Hence, the output torque can be controlled directly, which not

Manuscript received October 31, 2019; revised January 9, 2020; accepted February 13, 2020. Date of publication February 19, 2020; date of current version June 23, 2020. This work was supported by the National Nature Science Foundation of China under Grant 51907073. Recommended for publication by Associate Editor A. Muetze. *(Corresponding author: Chun Gan.)*

The authors are with the State Key Laboratory of Advanced Electromagnetic Engineering and Technology, School of Electrical and Electronic Engineering, Huazhong University of Science and Technology, Wuhan 430074, China (e-mail: zhiyueyu@hust.edu.cn; chungan@hust.edu.cn; cy_huster@hust.edu.cn; ronghaiqu@hust.edu.cn).

Color versions of one or more of the figures in this article are available online at http://ieeexplore.ieee.org.

Digital Object Identifier 10.1109/TPEL.2020.2975121

only improves the dynamic response, but also reduces the torque ripple in the SRM drive. However, since there is no definition of the turn-ON and turn-OFF angles, negative torque is easily generated, which will affect the efficiency of the SRM system. The excitation region is limited in the direct instantaneous torque control (DITC) scheme to avoid negative torque generation [32]–[36]. With the employment of the torque sharing function, driving signals can be obtained directly by the torque hysteresis controller, which can reduce the torque ripple. Nevertheless, the motor magnetic characteristic is required and the output torque capacity is reduced since the phase current drops rapidly in the commutation region.

Similar to the synchronous reluctance machine, the modular three-phase converter is adopted to realize sinusoidal bipolar current excitation in the SRM drive [37], [38]. Since the stator winding is excited by smooth sinusoidal current, the torque ripple and vibration caused by the current chopping can be reduced. It is proved in [39] that, the average torque for the SRM is mainly generated by the dc component, fundamental component, and second-order component of the stator current. Hence, when the SRM is only driven by the sinusoidal current, the torque output capacity will be decreased significantly. In [40], a hybrid excitation motor structure is put forward to improve the torque capacity. Although the rotor shape is similar to that in a conventional SRM, an additional dc winding is needed to generate the excitation magnetic field, which is different from that in conventional SRMs. Also, the working principle and corresponding control strategy to improve the motor performance are not proposed and analyzed in detail.

In [41], the pseudosinusoidal current excitation method is put forward. Based on the inductance profile, the reference value of the unipolar stator current is online optimized to minimize the torque ripple [42]. By applying the current hysteresis control, the calculated pseudosinusoidal current can be generated to drive the SRM. Nevertheless, the complex online calculation and the narrow speed range limit the industrial application of this control strategy. A more promising SRM drive should satisfy the following requirements:

1) the torque ripple and vibration should be reduced;
2) the efficiency and torque capability are not decreased;
3) no requirement for preknowledge of the motor magnetic characteristics;
4) relatively high robustness with fault-tolerant ability;
5) modular converter structure.

With the development of the flux modulation principle, several flux modulation motor topologies have been put forward, such as the flux reversal motor, the flux switching motor, and the vernier motor [43]. Flux modulation motors are developed from magnetic gearing motors, which contains a magnetic gear to amplify the output torque. The flux modulation motor is composed of three basic parts, including the excitation magnetic field generator, flux modulator, and armature magnetic field generator, and the working principles of the magnetic gear and flux modulation motor are approximately the same [44]. The flux modulator plays the role of a magnetic gear to reduce the rotating speed of the armature field and amplifies the output torque with the magnetic gear effect [45], [46]. Due to the introduction of the flux modulator, the torque performance can be greatly improved, which is the most significant advantage of flux modulation motors. Hence, considering these points, the flux modulation method can be further developed for SRMs to improve the motor performance.

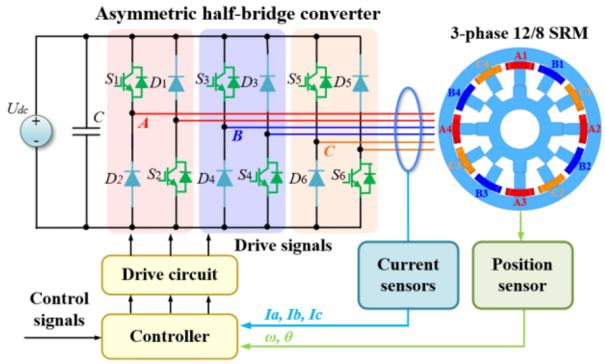

Fig. 1. Schematic diagram of the conventional three-phase SRM drive.

In order to reduce the torque ripple and vibration in three-phase SRMs, a novel current control technique with harmonic current suppression is proposed in this article based on a developed flux modulation principle. The working principle of the proposed SRM drive is analyzed in detail, including the excitation magnetic field, flux modulator, and armature magnetic field. A modular open-winding converter is developed, and the corresponding vector control scheme is presented, including the vector distribution and pulsewidth modulation (PWM) method. Furthermore, a harmonic current suppression method is proposed based on the vector proportional–integral (VPI) regulator. Compared to existing schemes, the torque ripple and vibration can be significantly decreased, without any sacrifice in the efficiency and torque output capacity. Also, because the prestored motor magnetic characteristics are not required, the computational burden will be significantly reduced. In terms of driving topology, a modular converter is employed for the proposed SRM drive, which can be applied to various applications conveniently. In addition, the introduction of the dc-biased current adds an additional control freedom degree, which can flexibly improve the fault-tolerant ability by changing the current direction due to the employment of the open-winding converter.

The organization of this article is as follows. In Section II, the conventional SRM drive is introduced. The working principle of the proposed SRM drive is investigated in Section III. In Section IV, the developed current control scheme is proposed and the harmonic current suppression strategy is put forward. Experimental results are carried out in Section V to verify the effectiveness of the proposed SRM drive. Finally, the conclusion is given in Section VI.

II. Conventional SRM Drives

The schematic diagram of the conventional three-phase SRM drive is shown in Fig. 1, which contains the 12/8 SRM, power converter, current sensors, position sensor, controller, and drive circuit. Each phase winding is driven by an isolated asymmetric

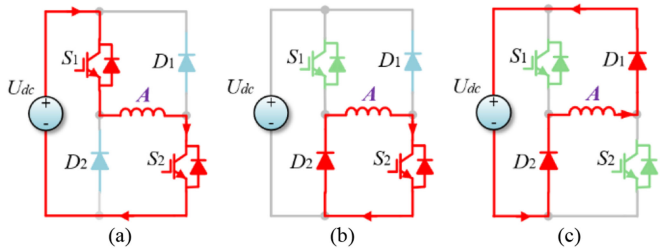

Fig. 2. Three switching states of conventional SRM drives. (a) Current rising state. (b) Freewheeling state. (c) Current falling state.

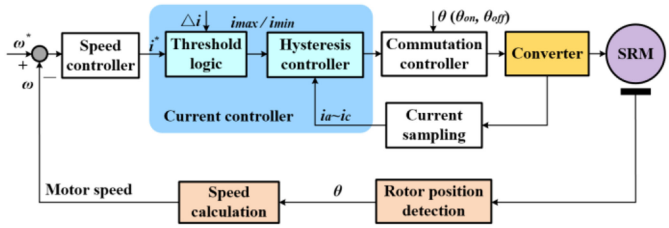

Fig. 3. Control diagram of the conventional SRM drive with CCC scheme.

half-bridge converter, including two switches and two diodes. Hence, unipolar discontinuous excitation currents will be generated independently, which ensures an excellent robustness and good fault-tolerant ability.

The voltage equation of the SRM can be expressed as follows:

$$U_m = R_s i_m + \frac{d\psi_m(i_m,\theta)}{dt} = R_s i_m + \frac{d[L_m(i_m,\theta)\cdot i_m]}{dt}$$
$$= R_s i_m + L_m(i_m,\theta)\frac{di_m}{dt} + i_m\omega_r\frac{\partial L_m(i_m,\theta)}{\partial\theta} \quad (1)$$

where R_s represents the stator resistance; ω_r represents the rotor speed; θ represents the rotor mechanical angle; U_m, i_m, ψ_m, and L_m represents the phase voltage, phase current, flux linkage, and phase inductance of the *m*-phase, respectively.

In conventional SRM drives, the working principle of the motor is based on the reluctance minimization principle, which differs from ac motors. Since the flux is always closed along the path with the smallest reluctance, electromagnetic torque will be generated by the tangential magnetic tension. The electromagnetic torque equation of the three-phase 12/8 SRM can be expressed as follows:

$$T_e = \sum_{m=1}^{3} T_{em} = \sum_{m=1}^{3} \frac{1}{2} i_m^2 \frac{\partial L_m(i_m,\theta)}{d\theta} \quad (2)$$

where T_e is the total electromagnetic torque, T_{em} is the phase torque. Hence, a positive electromagnetic torque can be generated when currents are injected separately in each phase during the ascending region of the phase inductance. The torque direction is not related to the current polarity since the torque is proportional to the square of the current.

The mechanical motion equation can be expressed as follows:

$$\frac{d(J\omega_r)}{dt} = T_e - T_L - D\omega_r - K\theta \quad (3)$$

where *J* is the moment of inertia of the SRM, T_L is the load torque, *D* is the damping coefficient, ω_r is the rotor mechanical speed, and *K* is the torsion elasticity coefficient.

For traditional SRM drives, the CCC strategy is usually employed [16], [17]. The operating states of the power converter are determined by the reference and feedback value of the phase current and the rotor position. Take phase A for example, three basic switching states and corresponding current paths are shown in Fig. 2. When the feedback current is smaller than the reference value, S_1 and S_2 are both turned ON, as shown in Fig. 2(a). The positive dc-link voltage is applied to the phase winding and the phase current rises rapidly. When the feedback current is larger than the reference value, S_1 is turned OFF and S_2 is ON, where a zero-voltage loop is applied to phase A winding, as shown in Fig. 2(b). In the phase turn-OFF region, S_1 and S_2 are both turned OFF, as shown in Fig. 2(c). The phase current falls rapidly to zero, due to the negative dc-link voltage applied to the phase winding.

Fig. 3 shows the control diagram of the conventional SRM drive with the CCC scheme. The rotor mechanical position is sampled by the position sensor to calculate the real-time speed and commutation logic. Current sensors detect phase currents for the hysteresis current controller. The speed controller, such as the proportional–integral (PI) controller, calculates the current reference $i_{\rm ref}$ based on the reference and feedback values of the rotor speed. The threshold logic block calculates the maximum current $i_{\max}$ (i.e., $i_{\max} = i_{\rm ref}+\triangle i$) and minimum current $i_{\min}$ (i.e., $i_{\min} = i_{\rm ref}\text{-}\triangle i$) according to the current reference $i_{\rm ref}$ and current hysteresis bandwidth $\triangle i$. The hysteresis controller compares the sampled phase currents and the maximum and minimum currents calculated by the hysteresis controller to determine the switching signal of each switch in the turn-ON region, aiming to keep the actual phase current between the maximum and minimum currents. The commutation controller is utilized to control the commutation logic from the turn-ON angle, turn-OFF angle, and sampled rotor position.

III. Developed Flux Modulation Principle for SRMs

For the flux modulation principle, the excitation magnetic field generator, flux modulator, and armature magnetic field generator are three basic units. Hence, the working principle of the proposed dc-biased sinusoidal current excited SRM drive can be analyzed in three parts as follows.

A. Excitation Magnetic Field Generator

In the proposed SRM drive, the three-phase stator currents contain both the ac component and dc-biased component, which can be expressed as follows:

$$\begin{cases} i_a = I_{ac}\sin(\theta_e) + I_{\rm dc} \\ i_b = I_{ac}\sin(\theta_e - \frac{2}{3}\pi) + I_{\rm dc} \\ i_c = I_{ac}\sin(\theta_e + \frac{2}{3}\pi) + I_{\rm dc} \end{cases} \quad (4)$$

where θ_e is the rotor electric angle; and $I_{\rm ac}$ and $I_{\rm dc}$ are the magnitude of ac and dc current components, respectively.

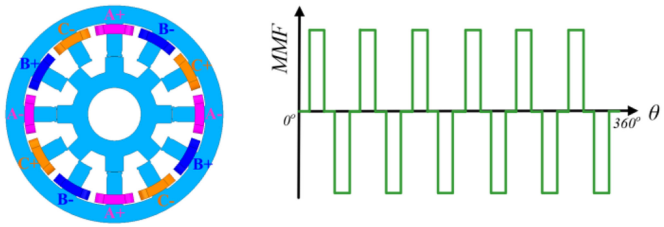

(a) (b)

Fig. 4. Diagram of the winding connection and stationary MMF in the proposed SRM drive. (a) Winding connection of the 12/8 SRM. (b) Stationary MMF diagram.

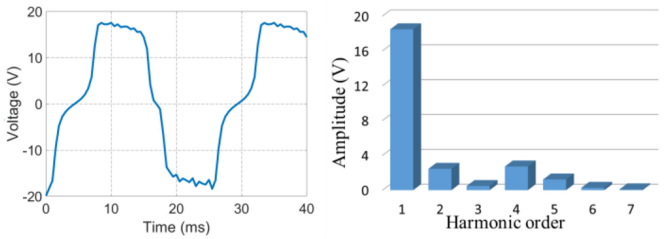

(a) (b)

Fig. 5. FEA result and FFT analysis of the back EMF. (a) Back EMF waveform. (b) FFT analysis.

In the proposed SRM drive, the dc-biased current component is the source of the excitation magnetic motive force (MMF). The diagram of the winding connection and the stationary MMF is shown in Fig. 4, where the symbols "+" and "–" represent the N and S polarities, respectively.

The mathematical expression of the stator excitation MMF can be expressed as follows:

$$F_f = \sum_{i=1}^{3,5,7,\ldots} F_i \sin(iP_{dc}\theta_s) = \sum_{i=1}^{3,5,7,\ldots} N_i I_{\mathrm{dc}} \sin\left(i\frac{N_s}{2}\theta_s\right) \quad (5)$$

where F_i is the *i*th harmonic component of the excitation MMF, P_{dc} is the pole pair number of the stationary MMF, N_s is the stator slot number, θ_s is the air gap mechanical angle, and N_i is the equivalent coil turns number of the stator winding of the *i*th harmonic component.

It can be seen that, since the winding polarity of two adjacent stator teeth is opposite, a static MMF will be established when dc-biased current components are fed into the three-phase stator winding, and the pole pair number is half of the stator slot number, which is equal to six in the 12/8 SRM. It is worth noting that since the stator windings on the adjacent stator teeth in the 12/8 SRM are wounded in opposite directions, the polarity of the dc-biased current component does not affect the operation of the SRM drive. Regardless of the polarity of the dc-biased current component, a six-polar-pair stationary MMF is generated.

Fig. 5 shows results of the finite element analysis (FEA) and fast Fourier transform (FFT) analysis of the phase back electromotive force (EMF), where the rotor speed is 300 r/min and I_{dc} is 10 A. In addition to the fundamental component, the phase back EMF also contains plenty of harmonic components, which will cause large harmonic current components, leading to torque ripple and vibration. Hence, it is necessary to investigate the harmonic current suppression strategy in the proposed SRM drive.

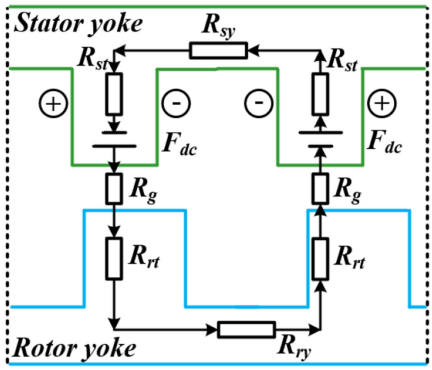

Fig. 6. Equivalent magnetic circuit diagram of the SRM in the proposed drive.

B. Flux Modulator

The distribution of the air-gap permeance will change when the rotor rotates, due to the doubly salient structure of the SRM. The equivalent magnetic circuit diagram is shown in Fig. 6, where R_{sy}, R_{st}, R_g, R_{rt}, and R_{ry} represent the magnetic resistance of the stator yoke, stator tooth, airgap, rotor tooth, and rotor yoke, respectively.

The air-gap permeance plays an important role in modulating the static excitation MMF. Considering the effect of the stator and rotor slotting, the mathematical equation of the permeance distribution caused by the stator and rotor slotting effects can be expressed as follows [47]:

$$\Lambda_s(\theta_s) = \Lambda_{s0} - \sum_{j=1}^{\infty} \Lambda_{sj} \cos(jN_s\theta_s) \quad (6)$$

$$\Lambda_r(\theta_s, t) = \Lambda_{r0} - \sum_{k=1}^{\infty} \Lambda_{rk} \cos\left[kN_r((\theta_s - \theta_0) - \omega_r t)\right] \quad (7)$$

where Λ_{s0} and Λ_{sj} are, respectively, the constant term and amplitude of the *j*th harmonic term of stator side permeance function, Λ_{r0} and Λ_{rk} are, respectively, the constant term and amplitude of the *k*th harmonic term of rotor side permeance function, N_r is the rotor teeth number, and θ_0 is the initial mechanical angle of the rotor.

Considering the superposition principle, the permeance of a doubly salient motor can be expressed as the interaction between the stator side permeance and rotor side permeance [48], [49]. The mathematical equation of the air-gap permeance can be obtained by using (6) and (7) as follows:

$$\Lambda_g(\theta_s, t) = \frac{\Lambda_s(\theta_s) \cdot \Lambda_r(\theta_s, t)}{\mu_0/g} \times \frac{\mu_0/g}{\Lambda_s(\theta_s) + \Lambda_r(\theta_s, t) - (g/\mu_0)\Lambda_s(\theta_s) \cdot \Lambda_r(\theta_s, t)} \quad (8)$$

where μ_0 represents the permeability of the vacuum and g represents the airgap length. For approximate calculation, (8) can be simplified in (9), where only the constant term and

fundamental term are considered

$$\begin{aligned}\Lambda_g(\theta_s,t) &= \Lambda_s(\theta_s)\cdot\Lambda_r(\theta_s,t)\Big/\frac{\mu_0}{g}\\ &\approx \underbrace{\Lambda_0}_{\text{(I)}} - \underbrace{\Lambda_{Ns}\cos(N_s\theta_s)}_{\text{(II)}} + \underbrace{\Lambda_{Nr}\cos(N_r\theta_s - N_r\omega_r t)}_{\text{(III)}}.\end{aligned} \tag{9}$$

It is obvious that the air-gap permeance can be divided into three parts. Part (I) is the constant term of air-gap permeance, which reflects the equivalent length of the air-gap. Part (II) is the static permeance term, which reflects the effect of stator slotting. Part (III) is the rotating permeance term, which reflects the effect of rotor slotting. The pole pair number of the rotating permeance is equal to the rotor teeth number, which is eight in the 12/8 SRM.

The excitation magnetic field is obtained by the mutual effect of the stationary excitation MMF and the air-gap permeance. Hence, according to (5) and (9), when the fundamental term of excitation MMF is only considered, the mathematical equation of the excitation magnetic field can be expressed as follows:

$$\begin{aligned}B_g(\theta_s,t) &= F_f(\theta_s)\cdot\Lambda_g(\theta_s,t)\\ &\approx \underbrace{N_1 I_{\rm dc}\sin\left(i\frac{N_s}{2}\theta_s\right)\cdot[\Lambda_0 - \Lambda_{Ns}\cos(N_s\theta_s)]}_{\text{(I)}}\\ &\quad + \underbrace{N_1 I_{\rm dc}\sin\left(i\frac{N_s}{2}\theta_s\right)\cdot\Lambda_{Nr}\cos(N_r\theta_s - N_r\omega_r t)}_{\text{(II)}}.\end{aligned} \tag{10}$$

In (10), the excitation magnetic field contains both the stationary part (I) and rotating part (II). It is known that only the rotating excitation magnetic field contributes to the electromechanical energy conversion. Thus, according to part (II) in (10), the pole pair number of the rotating excitation magnetic field can be obtained by the following:

$$P_B = |N_r - P_{\rm dc}| = \left|N_r - \frac{N_s}{2}\right|. \tag{11}$$

Hence, for the 12/8 SRM, after the flux modulation of the stator and rotor, a two-pole-pair air-gap rotating excitation field can be generated by the six-pole-pair excitation MMF.

C. Armature Magnetic Field Generator

In the proposed SRM drive, the ac component in the stator current is the source of the armature MMF. When the three-phase symmetric sinusoidal currents are injected into the three-phase symmetric stator winding, respectively, a rotating armature MMF will generate. The pole pair number of the rotating armature MMF is equal to the pole pair number of the stator winding.

According to the principle of the synchronous machine, to generate a constant electromagnetic torque, the speed and direction of the rotating armature MMF must be the same to the rotating excitation magnetic field. Hence, the pole pair number of the stator winding should satisfy

$$P_a = P_B = \left|N_r - \frac{N_s}{2}\right|. \tag{12}$$

For the winding connection in Fig. 4(a), the pole pair number of the stator winding is two by using the star of slot theory [50], which exactly satisfies the pole pair number relation in (12). Therefore, the 12/8 SRM can be considered as a kind of flux modulation machine and driven by the dc-biased sinusoidal current. The theoretic analysis above is suitable for all SRMs with 12 stator teeth and 8 rotor teeth, where this slot–pole combination is commonly used in three-phase SRMs.

D. Torque Ripple and Vibration Analysis

The instantaneous electromagnetic torque of the motor can be expressed as follows [49]:

$$T_e = \frac{e_a(t)i_a(t) + e_b(t)i_b(t) + e_c(t)i_c(t)}{\omega_r} \tag{13}$$

where $e(t)$ and $i(t)$ are the phase back EMF and current, respectively. It can be seen that the instantaneous electromagnetic torque can be obtained by the product of the instantaneous phase current and back EMF. The average torque is generated only when the harmonic order of the phase current is the same as that of the back EMF. Otherwise, the torque ripple will be generated.

According to Fig. 5, there are plenty of harmonic components in the phase back EMF, which are caused by the salient stator and rotor structure. Besides, in the conventional CCC scheme, the stator current is a discontinuous square-wave current, which also contains plenty of harmonic components. Hence, the interaction of the harmonic back EMF and harmonic current will cause the torque ripple.

In the proposed drive, based on the flux modulation principle, the dc-biased sinusoidal current is generated to drive the SRM. Hence, the harmonic current components in the stator current can be eliminated and the interaction of the harmonic back EMF and harmonic current can be reduced. As a result, the torque ripple can be decreased.

The average torque is mainly generated by the interaction of the fundamental components of the phase current and back EMF. The contribution of harmonic current components to the average torque is small compared to the fundamental component. Hence, the torque capability will not be decreased by employing the proposed control strategy with harmonic current suppression.

The vibration of the SRM is related to the fluctuation of the radial force. The interaction of the fundamental and harmonic magnetic fields will generate vibrations. In the conventional CCC scheme, the stator current is a discontinuous square-waveform, which contains plenty of harmonic components. The harmonic current components will generate plenty of harmonic magnetic fields in the airgap. Then, significant vibrations will be generated by the interaction of the fundamental and harmonic magnetic fields.

In the proposed scheme, since the SRM is driven by the dc-biased sinusoidal current, harmonic current components can be effectively eliminated. Harmonic magnetic field components

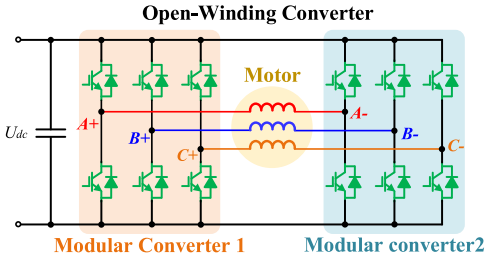

Fig. 7. Developed three-phase open-winding SRM converter.

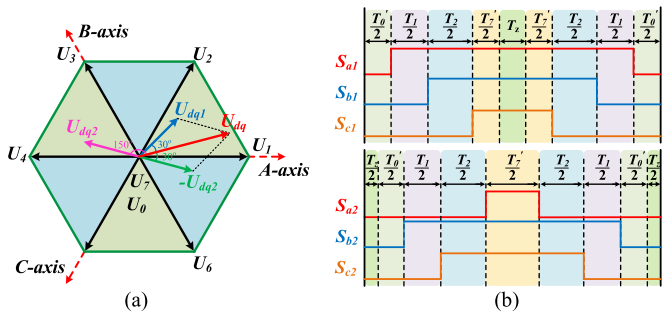

Fig. 8. Diagram of rotating voltage vectors and driving signals. (a) Relationship between the rotating voltage components of two converters. (b) Driving signals of two converters.

can also be significantly decreased and the vibration can be significantly reduced.

IV. Proposed Control Strategy Based on Open-Winding Converter

A. Novel Current Excitation Method

In a conventional ac motor drive, a two-level inverter is commonly used, because the stator winding is connected in star and the sum of phase currents is equal to 0 without zero-sequence current component. Thus, there are only ac components in the stator winding.

In the proposed drive, since the working principle of the SRM is based on the flux modulation principle, the dc-biased component is needed in the stator current to generate the excitation magnetic field and enhance the torque capability. Hence, the sum of phase currents is not equal to 0 and there should be a zero-sequence current flow path, which cannot be achieved by using only a two-level inverter. Thus, the open-winding converter is needed rather than a two-level inverter.

The open-winding converter topology of the proposed three-phase SRM drive is shown in Fig. 7. The output terminals of two modular three-phase converters are connected to the two ends of the three-phase stator winding, which constitute an open-winding converter. Hence, the voltage vector applied to the stator winding is synthesized by the voltage vector of the two inverter outputs. The relationship between the winding voltage vector and the voltage vector of each modular converter can be expressed as follows:

$$U_{\mathrm{ref}} = U_{\mathrm{ref1}} - U_{\mathrm{ref2}} \tag{14}$$

where U_{ref} represents the winding voltage vector, and U_{ref1} and U_{ref2} represent the voltage vectors of converters 1 and 2, respectively.

In order to produce the three-phase symmetric dc-biased sinusoidal current, the output voltage vector of two converters should contain both the rotating component and zero-sequence component. Hence, (12) can be further expressed as follows:

$$\begin{cases} U_{dq} = U_{dq1} - U_{dq2} \\ U_0 = U_{01} - U_{02} \end{cases} \tag{15}$$

where subscript *dq* and *0* represent the rotating component and zero-sequence component of each voltage vector, respectively.

Since two modular converters share one dc voltage source, the rotating component of the output voltage vector in the two converters should have a 120° phase-shift angle to avoid the generation of third-order harmonic voltage [51]. Fig. 8(a) shows the relationship of the rotating component of three voltage vectors. U_0–U_7 represents the eight fundamental vectors, respectively. The amplitude of U_{dq1} and U_{dq2} are equal, which is 0.57735 times of the amplitude of U_{dq}. Besides, U_{dq1} and U_{dq2} lead U_{dq} 30° and 150° degree electric angle, respectively.

For conventional two-level space vector pulsewidth modulation (SVPWM), the equivalent voltage vector is composed of two effective vectors and two zero vectors in each sampling period. Since the zero-sequence current path does not exist, the action time of two zero vector is equal. Therefore, the action time of each vector can be expressed as follows:

$$\begin{cases} T_s = T_1 + T_2 + T_0 + T_7 \\ T_0 = T_7 = \frac{T_s - T_1 - T_2}{2} \end{cases} \tag{16}$$

where T_s represents the PWM period; T_1 and T_2 represent the action time of two effective vectors; T_0 and T_7 represent the action time of U_0 and U_7, respectively.

Due to the zero-sequence current path in the open-winding converter, the action time assignment of zero vectors is determined by the zero-sequence component of the voltage vector. If the action time of U_7 is longer than that of U_0 in converter 1 and shorter than that of U_0 in converter 2, the positive zero-sequence voltage will generate in the winding voltage vector. Fig. 8(b) shows the diagram of driving signals of two converters in the proposed SRM drive. T_z represents the equivalent action time of the zero-sequence voltage component, which can be obtained as follows:

$$T_z = \frac{|U_{01}|}{U_{\mathrm{dc}}} = \frac{|U_{02}|}{U_{\mathrm{dc}}} = \frac{|U_0|}{2U_{\mathrm{dc}}}. \tag{17}$$

Therefore, in order to generate positive zero-sequence voltage component in the winding voltage vector, the zero-vector action time of two converters can be redistributed as follows:

$$\begin{cases} T_0' = T_7' = (T_s - T_1 - T_2 - T_z)/2 & \text{(converter 1, 2)} \\ T_0 = T_0', T_7 = T_7' + T_z & \text{(converter 1)} \\ T_0 = T_0' + T_z, T_7 = T_7' & \text{(converter 2).} \end{cases} \tag{18}$$

It can be seen that the zero-sequence component of two inverters has opposite polarity. The diagram of U_{ref}, U_{ref1}, and

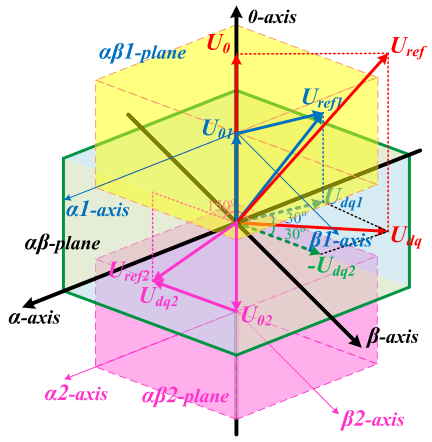

Fig. 9. Diagram of three voltage vectors in $\alpha\beta 0$-axis.

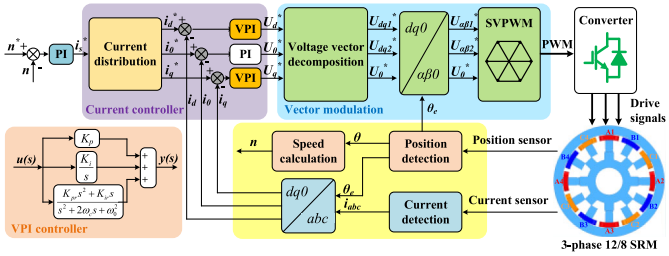

Fig. 10. Control diagram of the proposed three-phase SRM drive.

U_{ref2} in $\alpha\beta 0$-axis is shown in Fig. 9. U_{ref} can be generated by the interaction of U_{ref1} and U_{ref2}. As shown in Fig. 9, the rotating component of the output voltage vector in the two converters should have a 120° phase shift. Hence, the amplitudes of the rotating component of two converter voltage vectors are equal, which is 0.57735 times of the amplitude of the rotating component of winding voltage vector. Besides, the rotating component of two converter voltage vector should lag the rotating winding voltage vector by 30° and 150°, respectively. Because the zero-sequence voltage component of the winding voltage vector is equally divided, the zero-sequence components of two converter voltage vectors are equal to half of the zero-sequence winding voltage component. Therefore, the relationship between the reference voltage vector of two modular converters and the winding voltage vector reference can be expressed as follows:

$$\begin{cases} U_{dq1}^{*} = \frac{\sqrt{3}}{3} U_{dq}^{*} e^{-j30^{o}} \\ U_{dq2}^{*} = \frac{\sqrt{3}}{3} U_{dq}^{*} e^{-j150^{o}} \\ U_{01}^{*} = -U_{02}^{*} = \frac{1}{2} U_{0}^{*}. \end{cases} \tag{19}$$

Therefore, when the reference voltage vector of the winding is determined, the reference voltage vectors of converters 1 and 2 can be obtained by using the relationship in Fig. 9 to decompose the winding reference voltage vector.

The control diagram of the proposed three-phase SRM drive is illustrated in Fig. 10. The root mean square (rms) value of the phase current is obtained by the PI-based speed regulator.

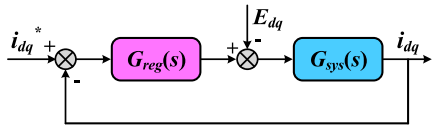

Fig. 11. Schematic diagram of the current close-loop controller.

The current distribution block is used to calculate the reference value of *dq0*-axis current based on the RMS value of the phase current obtained by the PI-based speed regulator. Since the *d*-axis current makes no contribution to the output torque, the *d*-axis reference current is set to zero. Hence, the RMS value of the phase current can be expressed as follows:

$$i_s = \sqrt{\left(\frac{i_q}{\sqrt{2}}\right)^2 + i_0^2}. \tag{20}$$

For the comprehensive consideration of the output torque capability and torque ripple reduction, the current ratio between the *q*-axis current and *0*-axis current is set to 1 in the current distribution block for a proof-of-concept. Hence, by substituting the current ratio into (20), the relationship among the phase current RMS value, *0*-axis current, and *q*-axis current can be expressed as follows:

$$\begin{cases} i_d^{*} = 0 \\ i_q^{*} = i_0^{*} = \sqrt{\frac{2}{3}} i_s^{*}. \end{cases} \tag{21}$$

According to (21), the reference value of the *dq0*-axis current can be obtained. The phase currents are sampled by Hall-effect current sensors. By using Park transformation, the actual *dq0*-axis current can be calculated according to the three-phase current and rotor position. The errors between the reference and actual value of *dq0*-axis currents are sent to the current regulator to calculate the reference value of the winding voltage vector in the *dq0*-axis. Because the *0*-axis current is not affected by the harmonic back EMF, the conventional PI regulator is selected for *0*-axis current regulation. However, the harmonic back EMF will generate significant three-order harmonic currents in the *dq*-axis. Hence, the VPI regulator is adopted in the *dq*-axis current regulator in the proposed drive. Based on the relationship in Fig. 9 and (19), the voltage vector decomposition block is used to calculate reference voltage vectors of two three-phase modular converters according to the winding voltage vector reference U_{dq0}^{*}. Furthermore, a harmonic current suppression strategy is employed to reduce the torque ripple and vibration, which will be analyzed in detail in the following part.

B. Harmonic Current Suppression Strategy

The schematic diagram of the current closed-loop controller is shown in Fig. 11, where E_{dq} represents the back EMF in the *dq*-axis, and $G_{\mathrm{reg}}(s)$ and $G_{\mathrm{sys}}(s)$ represent the transfer function of the current regulator and motor system in the *s*-domain. For the SRM drive, the transfer function of the motor system can be

expressed as follows:

$$G_{\text{sys}}(s) = \frac{1}{sL_s + R_s} \tag{22}$$

where s represents the Laplace operator, L_s is the stator inductance, and R_s is the stator resistance.

As shown in Fig. 5(b), because there are plenty of second and fourth harmonic component in the phase back EMF, third harmonic component will generate in E_{dq} after park transformation. Therefore, the third harmonic current in the *dq*-axis will generate, which affects the SRM control performance. Hence, in the proposed SRM drive, the harmonic current suppression scheme should be further developed in the current controller to improve the performance of the control system.

In conventional motor drives, the PI regulator is commonly used, and the transfer function of the PI regulator can be expressed as follows:

$$G_{\text{PI}}(s) = K_p + \frac{K_i}{s} \tag{23}$$

where K_p represents the proportional coefficient and K_i represents the integral coefficient. However, PI regulator has poor control ability to ac signals due to the low high-frequency gain of the PI controller, which means that the PI regulator cannot eliminate the harmonic current caused by harmonic back EMF.

In order to eliminate the harmonic current in the proposed SRM drive, the VPI current regulator is developed. The transfer function of the VPI regulator can be expressed as follows:

$$G_{\text{VPI}}(s) = \underbrace{K_p + \frac{K_i}{s}}_{\text{I}} + \underbrace{\frac{K_{pr}s^2 + K_{ir}s}{s^2 + \omega_b s + \omega_0^2}}_{\text{II}} \tag{24}$$

where K_{pr} is the second-order resonant coefficient, K_{ir} is the first-order resonant coefficient, ω_b is the resonant bandwidth, and ω_0 is the resonant angular frequency. It can be seen that the VPI regulator can be divided into two parts. Part (I) is the PI term, which is equal to a conventional PI regulator. Part (II) is the resonant term, which contains a second-order resonant term and a first-order resonant term. The additional resonant term provides a high gain at the resonant frequency. Hence, the resonant-frequency signal can be tracked accurately. For 12/8 SRMs, to eliminate the third order harmonic current component in the *dq*-axis, the resonant angular frequency should be equal to the frequency of third order harmonic current component, given by

$$\omega_0 = 3 \cdot N_r \cdot \omega_r = 24\omega_r. \tag{25}$$

Compared to the conventional PI regulator, additional resonant terms greatly increase the calculation complexity. In order to simplify the calculation, a method to realize resonance calculation by using two integrators is employed in this article. By splitting the transfer function of the resonant term, the second-order resonant term and first-order resonant term in the VPI regulator can be realized through two integrators, as shown in Fig. 12. By adopting the simplified method, both the resonant frequency and resonant bandwidth can be expressed as a simple form of gain, respectively. Hence, when the SRM

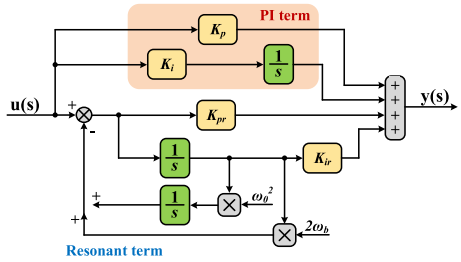

Fig. 12. Block diagram of the VPI regulator based on two integrators.

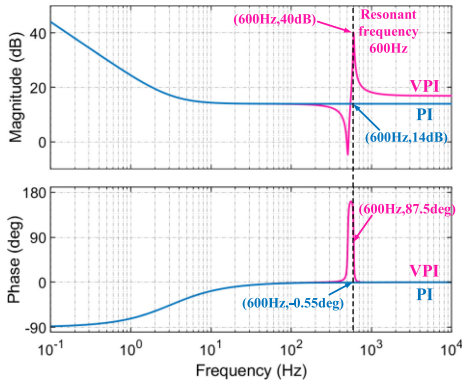

Fig. 13. Bode diagram of the PI and VPI regulators.

operates in the dynamic process, the resonant frequency and resonant bandwidth can be calculated and updated in real time, which improves the performance of the current regulator in the dynamic process. Furthermore, because the resonant term is separated into two integrators, online calculation of the accurate trigonometric function can be avoided, making the discrete process of transfer function in the *s*-domain much simpler for the digital controller.

The bode diagram of the PI and VPI regulators are shown in Fig. 13, where K_p is 5, K_i is 100, K_{pr} is 2, K_{ir} is 400, ω_0 is 1200π, and ω_b is 12π. It can be seen that both the PI and VPI regulators have large low-frequency gain, which ensures a good regulation ability for the dc component. However, at the resonant frequency, the VPI regulator achieves a larger gain to regulate the ac component compared to the PI regulator, which can be used to suppress the third harmonic current in the *dq*-axis. Because the SRM is an inductive load, phase delay will be introduced into the control system. The VPI regulator has a phase lead angle of 87.5° at the resonant frequency, which is beneficial to compensate the phase delay caused by the SRM.

From (22)–(24), the transfer function of the open-loop current controller based on the PI and VPI regulators can be expressed as follows:

$$G_{\text{open\_PI}}(s) = G_{\text{sys}}(s)G_{\text{PI}}(s) = \frac{K_p s + K_i}{s^2 L_s + sR_s} \tag{26}$$

$$G_{\text{open\_VPI}}(s) = G_{\text{sys}}(s)G_{\text{VPI}}(s) = \frac{(K_p+K_{pr})s^3+(K_p\omega_b+K_i+K_{ir})s^2+(K_i\omega_b+K_p\omega_0^2)s+K_i\omega_0^2}{s(s^2+\omega_b s+\omega_0^2)(sL_s+R_s)}. \tag{27}$$

TABLE I
COMPARING OF PROPOSED AND EXISTING SRM CONTROL STRATEGY

Item \ Method	Method in [16] and [17]	Method in [29]-[31]	Method in [32]-[36]	Method in [37] and [38]	Method in [41] and [42]	Proposed method
Torque ripple	Large	Medium	Small	Small	Small	Small
Vibration	Large	Medium	Small	Small	Small	Small
Motor magnetic characteristics	Not required	Required	Required	Not required	Required	Not Required
Efficiency	High	Low	Medium	Low	Medium	High
Output torque capacity	High	Low	Low	Low	Medium	High
Fault-tolerant ability	Medium	Medium	Medium	Without	Low	High
Computational complexity	Easy	Complicated	Complicated	Medium	Complicated	Medium
Modular converter	Not equipped	No equipped	Not equipped	Equipped	Not equipped	Equipped

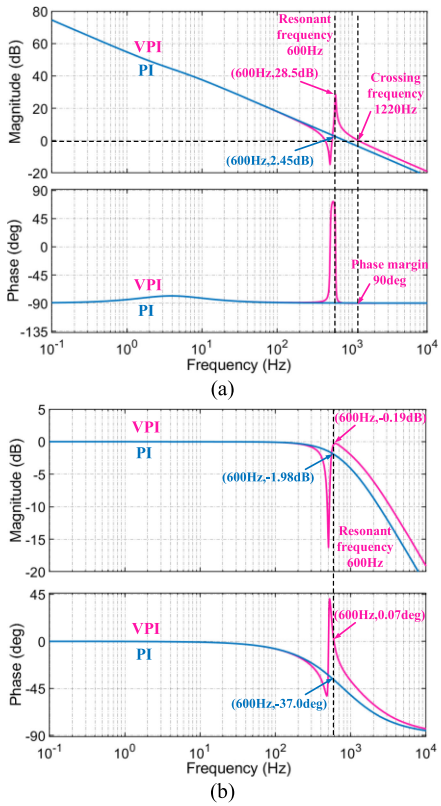

Fig. 14. Bode diagram of the current controller. (a) Open-loop system. (b) Closed-loop system.

Fig. 14(a) shows the bode diagram of the open-loop current controller. The stability of the system can be characterized by the phase margin of the open-loop controller. It can be seen from Fig. 14 that the crossing frequency of the open-loop controller in the proposed drive is 1220 Hz and the phase margin is 90°. Hence, the VPI regulator can always remain stable during the working process. Besides, the gain of the open-loop controller will not obviously decrease by an appropriate resonant bandwidth with the deviation of resonant frequency, which ensures the harmonic current suppression ability in the system dynamic process.

Fig. 14(b) shows the bode diagram of the closed-loop current controller. For the PI-based current controller, the closed-loop gain at the resonant frequency is –1.98 dB, and the phase response is –37°. Hence, the third harmonic current in the *dq*-axis cannot be effectively suppressed by the PI current controller. However, for both the dc component and resonant frequency component, the VPI current controller can ensure the 0 dB gain and 0° phase response, so that the amplitude and phase between the reference and actual signal are the same, which means that the VPI current controller can achieve excellent harmonic current suppression ability.

C. Comparison With Existing Strategies

A detailed comparison of existing and proposed control strategies is summarized in Table I. The proposed scheme is compared with five existing methods, including the CCC, DTC, DITC, bipolar sinusoidal current excited, and pseudosinusoidal current excited schemes. Comparisons of existing methods have already been made in previous papers, which are explained in detail as below. For further explanation, the experimental results under the typical CCC and pure-sinusoidal current excited schemes have been carried out for comparison in Section V.

The CCC scheme is commonly adopted in the SRM drive due to the advantage of simple calculation [16], [17]. However, because the hysteresis current controller is employed, the switching frequency is uncertain and the phase current is a discontinuous square-waveform, which contains a large number of chopping ripples. Hence, the torque ripple and vibration will be generated.

In [18], [29]–[31], the DTC scheme is developed in SRM drives to reduce the torque ripple. The torque and magnetic flux hysteresis controllers are employed to obtain the output voltage vector of the power converter directly. It is proved that, compared with the traditional CCC scheme, the DTC scheme can effectively reduce the torque ripple of the SRM [52]. However, since there is no definition of turn-ON and turn-OFF angles of each phase, negative torque is easily generated, which will affect the motor system efficiency [53], [54].

In order to reduce the torque ripple and avoid the negative torque generation, the DITC scheme is investigated in [32]–[36]. Compared with the DTC scheme, the excitation region of each phase is limited by the predefined turn-ON and turn-OFF angles to avoid the negative torque generation in the DITC scheme [53]. Hence, the torque-ampere ratio in the DITC scheme is larger than that in the DTC scheme [54]. In [32] and [33], the DITC

scheme is compared with the traditional CCC scheme, where the torque ripple can be reduced significantly. However, in both the DTC and DITC schemes, since the torque is controlled directly, the actual torque should be observed in real time according to the current and rotor position in a torque table, where accurate motor magnetic characteristics are required [36]. Besides, due to the introduction of torque sharing function, the phase current decreases significantly in the commutation region, where the output torque capability of the SRM is reduced.

In [41] and [42], the pseudosinusoidal current excitation method is put forward. Based on the inductance profile, the reference value of the stator current is online optimized to minimize the torque ripple. By applying the current hysteresis controller, switching signals can be obtained by comparing the calculated pseudosinusoidal current and sampled phase current. Since the phase current is smooth and optimized, the torque ripple can be reduced compared with the CCC, DTC, and DITC schemes [42], [53]. However, because the reference current is calculated based on the inductance profile, accurate motor magnetic characteristics are needed and the real-time calculation is complicated.

Similar to the synchronous reluctance motor, a bipolar sinusoidal current excited SRM drive is proposed in [37] and [38]. Since the stator winding is excited by a smooth pure-sinusoidal current, the torque ripple and vibration caused by the high-frequency harmonic current components can be reduced. However, it is proved in [39] that the average torque for the SRM is mainly generated by the dc component, fundamental component, and second-order component of the stator current. Hence, when the SRM is only driven by the pure-sinusoidal current, the torque capacity is decreased significantly.

This article proposes a dc-biased sinusoidal current excited SRM drive. Different from the existing control strategy mentioned above, the working principle of the proposed SRM control scheme is based on the flux modulation principle. The low-frequency harmonic components and high-frequency ripple in the dc-biased sinusoidal phase current are effectively suppressed, and the torque ripple and vibration of the motor can be significantly reduced. Furthermore, the torque capacity can be enhanced by the dc-biased current component, so that the efficiency of the SRM drive can be ensured. Besides, because the polarity of the dc-biased current component does not affect the operation of the SRM, the fault-tolerance operation can be realized with the open-circuit fault of the power switch, by changing the polarity of the dc-biased current component. Moreover, the modular converter is equipped in the proposed SRM drive, which shows a great potential for industrial application.

TABLE II
MOTOR PARAMETERS

Parameters	Unit	Value
Phase number	-	3
Number of stator poles	-	12
Number of rotor poles	-	8
Rated power	kW	1
Rated speed	r/min	1500
Phase resistance	mΩ	40
Minimum phase inductance	mH	0.19
Maximum phase inductance	mH	2.02
Stator arc angle	deg	15
Rotor arc angle	deg	19
Air gap length	mm	0.3

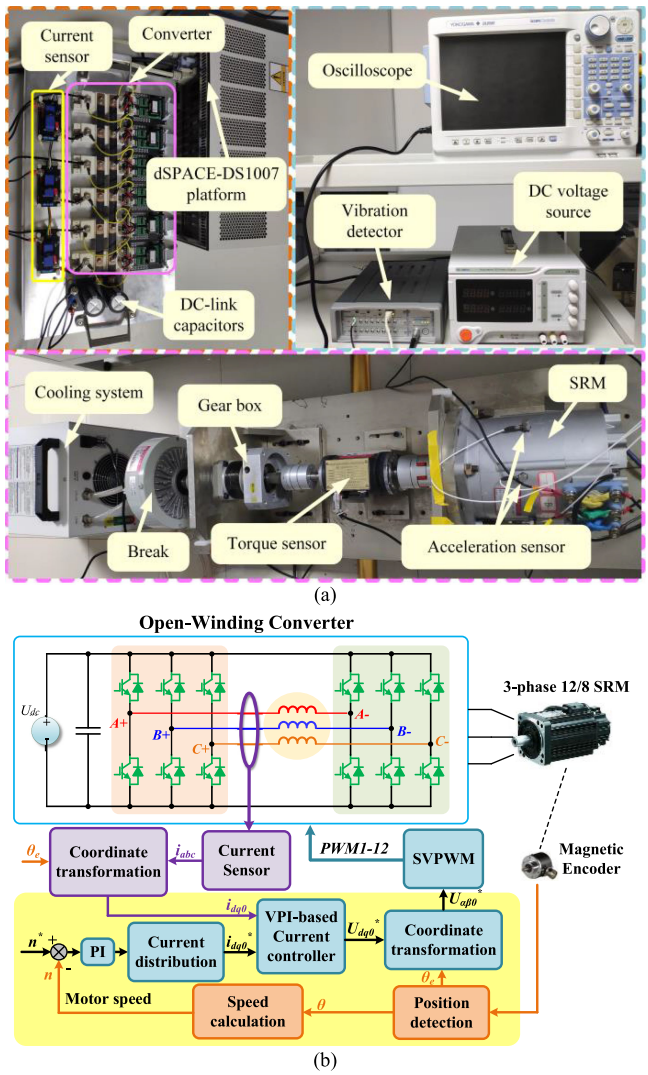

Fig. 15. Experimental setup. (a) Experimental equipment. (b) Schematic diagram of the proposed SRM drive.

V. EXPERIMENTAL RESULTS

In order to test the performance of the proposed SRM drive, experimental verifications are carried out on a three-phase 12/8 SRM prototype. The main parameters are listed in Table II. The experimental equipment and the schematic diagram of the system are shown in Fig. 15. The digital control program is implemented by a dSPACE DS1007 platform. The PI and proposed VPI-based control schemes are employed to regulate the speed and current, respectively. A multichannel isolated oscilloscope is adopted to record experimental waveforms. The phase currents are sampled by Hall-effect current sensors LA55P/SP1, and the rotor position and mechanical speed are detected by a magnetic encoder installed on the rotor. The torque waveform is observed by using the real-time phase currents and rotor position to look

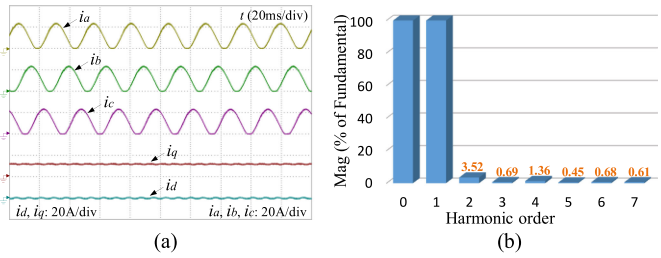

Fig. 16. Experimental results at 300 r/min without the proposed harmonic current suppression strategy. (a) Three-phase currents and *dq*-axis currents. (b) FFT analysis of the phase current.

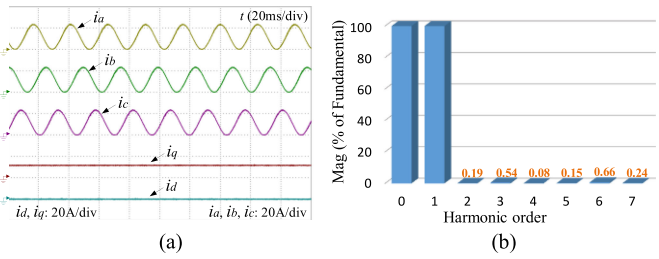

Fig. 17. Experimental results at 300 r/min with the proposed harmonic current suppression strategy. (a) Three-phase currents and *dq*-axis currents. (b) FFT analysis of the phase current.

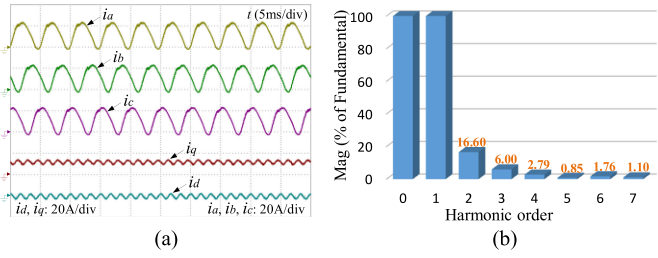

Fig. 18. Experimental results at 1500 r/min without the proposed harmonic current suppression strategy. (a) Three-phase currents and *dq*-axis currents. (b) FFT analysis of the phase current.

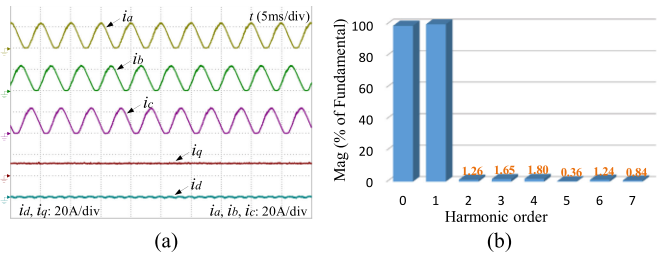

Fig. 19. Experimental results at 1500 r/min with the proposed harmonic current suppression strategy. (a) Three-phase currents and *dq*-axis currents. (b) FFT analysis of the phase current.

up for the prestored torque table that includes the torque-current-position characteristics. Acceleration sensors are installed on the motor frame to detect the motor vibration. The open-winding converter is adopted to drive the SRM and a programmable dc voltage source is employed to provide the dc-link voltage. The switching frequency and the current sampling frequency are both set to 10 kHz. For the motor test platform, a magnetic brake is used to provide the load torque, and a gearbox is connected between the motor and magnetic brake to amplify the output torque.

Figs. 16 and 17 show the experimental results of three-phase currents, *dq*-axis currents, and corresponding FFT analysis at 300 r/min and 1.5 N·m with and without the proposed harmonic current suppression method, respectively. In the figure, i_a, i_b, and i_c are the stator currents of phases A, B, and C, respectively, and i_d and i_q are the *d*-axis current and *q*-axis current, respectively. It can be seen from Fig. 16(a) that, the three-phase current contains large harmonic components without the harmonic current suppression strategy, leading to current distortion. The harmonic component in three-phase current will lead to a large third order harmonic component in the *dq*-axis current after the coordinate transformation, leading to poor current tracking control due to the third order harmonic component in the *dq*-axis current. The high-frequency harmonic components cannot be eliminated by the conventional PI regulator without the proposed harmonic suppression strategy. By applying the proposed harmonic suppression method, a large gain at the resonant frequency can be achieved due to the developed VPI regulator. Hence, the harmonic components in the three-phase current and *dq*-axis current can be significantly suppressed, as shown in Fig. 17(a).

Figs. 16(b) and 17(b) show the FFT analysis of the phase current. Without the proposed harmonic suppression strategy, the amplitudes of the second-, third-, fourth-, fifth-, sixth-, and seventh-order harmonic current components are 3.52%, 0.69%, 1.36%, 0.45%, 0.68%, and 0.61% of the fundamental component amplitude, respectively, where the total harmonic distortion (THD) is 6.9%. By employing the proposed harmonic current suppression method, the amplitudes of the second-, third-, fourth-, fifth-, sixth-, and seventh-order harmonic current components can be reduced to 0.19%, 0.54%, 0.08%, 0.15%, 0.66%, and 0.24% of the fundamental component amplitude, respectively, where the THD is greatly reduced to only 3.0%.

Experiments are also carried out at 1500 r/min and 1.5 N·m with and without the proposed harmonic current suppression method, as shown in Figs. 18 and 19. It can be seen that the distortion of the phase current is much more serious at higher speed. The amplitudes of the second-, third-, fourth-, fifth-, sixth-, and seventh-order harmonic current components are 16.6%, 6.00%, 2.79%, 0.85%, 1.76%, and 1.10% of the fundamental component amplitude, respectively, where the THD is 18.44%. However, by employing the proposed harmonic suppression method, the harmonic components in both the phase current and *dq*-axis current can still be well eliminated, where the amplitudes of the second-, third-, fourth-, fifth-, sixth-, and seventh-order harmonic current components can be reduced to 1.26%, 1.65%, 1.80%, 0.36%, 1.24%, and 0.84% of the fundamental component amplitude, respectively, where the THD can be reduced to 5.10%. Therefore, experimental results prove that the harmonic current caused by the distorted back EMF can be effectively suppressed by using the proposed VPI-based harmonic current suppression method for the developed SRM drive.

Fig. 20 shows the experimental results of three-phase current and output torque at 300 r/min and 1.5 N·m with the conventional

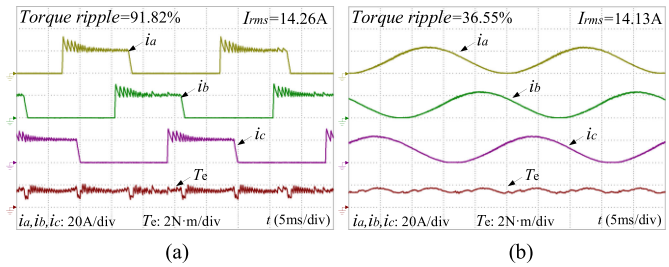

Fig. 20. Experimental results of three-phase current and output torque at 300 r/min under different control methods. (a) Conventional CCC method. (b) Proposed control method.

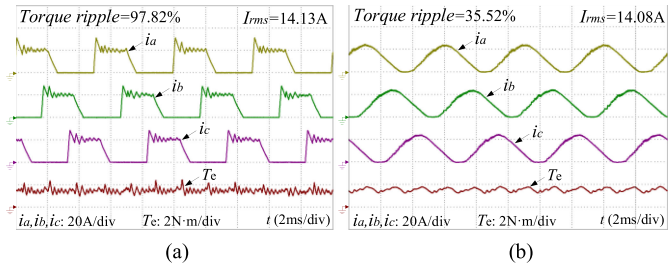

Fig. 21. Experimental results of three-phase current and output torque at 1500 r/min under different control methods. (a) Conventional CCC method. (b) Proposed control method.

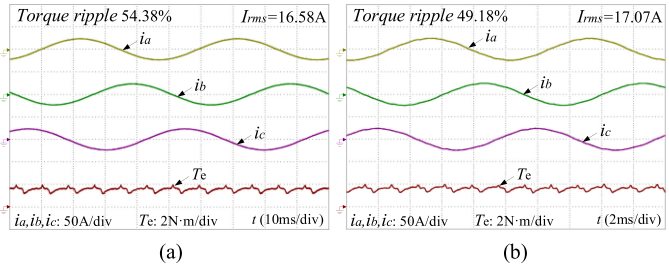

Fig. 22. Experimental results of three-phase current and output torque at 300 and 1500 r/min under pure-sinusoidal current excited method. (a) 300 r/min. (b) 1500 r/min.

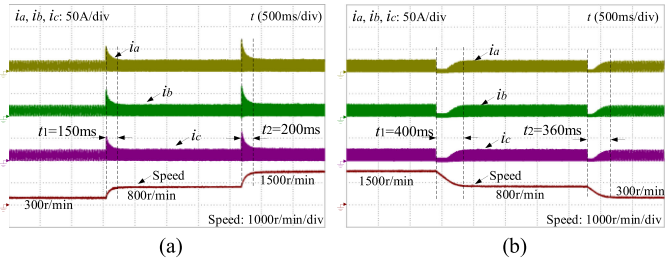

Fig. 23. Experimental waveforms of three-phase current and actual rotor speed under speed change. (a) Speed-up condition. (b) Speed-down condition.

CCC method and proposed control method. When the CCC scheme is adopted, the phase current waveform is a square waveform, which contains a large amount of harmonic components. The introduction of current hysteresis control also causes a large amount of high-frequency current ripple. The harmonic current and high-frequency current ripple will both lead to large torque ripple. During the phase commutation process, the torque will drop due to the discontinuous phase current, which also increases the torque ripple of the SRM.

In the proposed scheme, the electromagnetic torque is generated by the interaction of the excitation magnetic field and the armature magnetic field, which differs from that in the conventional CCC scheme. The current harmonic components can be greatly reduced with continuous dc-biased sinusoidal current. The torque ripple caused by the harmonic current component, high-frequency current ripple, and phase commutation can be effectively eliminated. By employing the proposed control strategy, the torque ripple can be reduced from 91.82 to 36.55%.

Fig. 21 represents the experimental results at 1500 r/min with different control schemes. It can be seen that the torque ripple can be reduced from 97.82% to 35.52%, and the RMS value of the phase current is nearly the same between the CCC and proposed schemes. Thus, the efficiency and output torque capacity will not decrease with the reduction of torque ripple by using the proposed strategy.

Fig. 22 shows the experimental results of three-phase current and output torque at 300 and 1500 r/min with the pure-sinusoidal current excited method. Stator windings are connected in star and three-phase symmetric pure-sinusoidal currents are generated to drive the SRM, which is similar to the synchronous reluctance motor. Compared with the conventional CCC scheme, the torque ripple can be reduced from 91.82% to 54.38% and 97.82% to 49.18% at 300 and 1500 r/min, respectively.

However, by employing the proposed flux modulated scheme, the torque ripple can be further reduced. Compared with the pure-sinusoidal excited scheme, the torque ripple in the proposed scheme can be further reduced to 36.55% and 35.52% at 300 and 1500 r/min, respectively. Besides, the RMS value of the phase current in the proposed scheme is smaller than that in the pure-sinusoidal current excited scheme. Therefore, compared with the sinusoidal current excited scheme, the torque capability can be increased with the reduction of torque ripple by using the proposed scheme.

The settling time of the motor drive can be represented by the response time to a step change of the speed reference. Fig. 23 illustrates the dynamic performance of the proposed SRM drive. As shown in Fig. 23(a), when the motor speed increases from 300 to 800 r/min and from 800 to 1500 r/min, the actual rotor speed reaches the steady-state for only 150 and 200 ms, respectively. It is clear that when the rotor speed increases, the proposed SRM drive can achieve fast dynamic performance. Besides, the experimental result under the speed decreasing condition is shown in Fig. 23(b). When the reference speed decreases from 1500 to 800 r/min and from 800 to 300 r/min, the actual rotor speed can also track the reference well, achieving a fast dynamic performance. The settling time of the proposed driving system can meet the requirement of the dynamic performance in the motor drive.

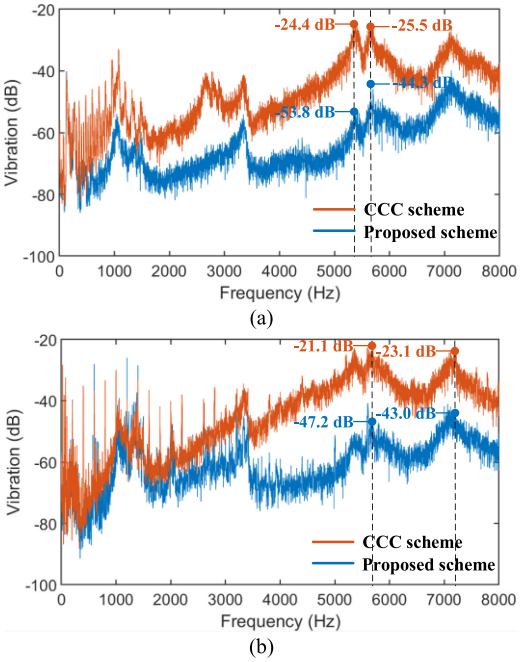

Fig. 24. Experimental waveforms of the vibration under the conventional CCC scheme and the proposed scheme under different rotor speed. (a) 300 r/min. (b) 1500 r/min.

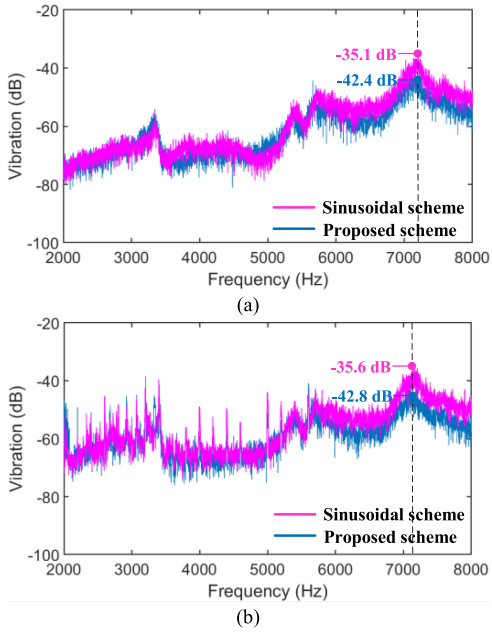

Fig. 25. Experimental waveforms of the vibration under the sinusoidal current excited scheme and the proposed scheme under different rotor speed. (a) 300 r/min. (b) 1500 r/min.

Fig. 24(a) shows the comparison of the vibration acceleration at 300 r/min with the traditional CCC and proposed scheme. In the CCC scheme, due to the high-frequency harmonic components contained in the square-wave phase current, the mechanical resonance phenomenon will occur. Therefore, a lot of high-frequency vibration will be generated. However, in the proposed scheme, the high-frequency harmonic current components are effectively eliminated, and thus the high-frequency vibration can be significantly reduced. The first significant vibration point in the CCC scheme is the 5370 Hz component, with an amplitude of –24.4 dB. By employing the proposed control scheme, the 5370 Hz vibration component can be reduced to –53.8 dB. The second significant vibration is the 5660 Hz component, which can be reduced from –25.5 to –44.3 dB by adopting the proposed scheme.

Fig. 24(b) shows the experimental results at 1500 r/min. The first and second significant vibration can be reduced from –21.1 to –47.2 dB and –23.1 to –43.0 dB, respectively. Besides, the RMS value of the vibration can be reduced from 1.067 to 0.143 g and from 1.682 to 0.208 g at 300 and 1500 r/min, respectively. It is obvious that, compared with the conventional CCC scheme, the proposed method has better high-frequency vibration suppression capability.

Fig. 25 shows the comparison of the vibration acceleration with the pure-sinusoidal current excited scheme and proposed scheme. By adopting the proposed scheme, the first significant vibration under 300 and 1500 r/min can be reduced from –35.2 to –42.4 dB and –35.6 to –42.8 dB, respectively. Besides, the RMS value of the vibration can be reduced from 0.232 to 0.143 g and 0.272 to 0.208 g at 300 and 1500 r/min, respectively. Although the pure-sinusoidal current excited scheme can reduce the vibration compared to the conventional CCC scheme, the proposed scheme still has better performance in terms of the vibration reduction compared to the pure-sinusoidal current excitation scheme.

Compared to the traditional CCC scheme, because the low-order harmonic current and high-frequency current ripple are significantly reduced, the proposed scheme can significantly reduce the torque ripple and vibration in the SRM drive while maintaining the torque output capability. Compared to other low-torque-ripple schemes, such as the DTC and DITC scheme, the motor magnetic characteristics are not required, and the online calculation can be simplified, without torque loss. Furthermore, the proposed SRM drive can be achieved by employing the modular three-phase converter, which is suitable for industrial applications.

VI. Conclusion

This article proposes a dc-biased sinusoidal current excited SRM drive by employing the developed flux modulation principle, aiming to reduce the torque ripple and vibration. Based on the open-winding converter topology, the SRM is driven by the dc-biased sinusoidal current, where the torque ripple and vibration caused by the harmonic current can be effectively reduced. In this article, based on the flux modulation principle, the working principle of the proposed SRM drive is first analyzed in detail. The dc-biased sinusoidal current generation strategy and the corresponding SVPWM modulation method is put forward. Then, to eliminate the low-order harmonic current caused by the distorted back EMF, a developed VPI-based current controller and the associated simplified implementation method is further presented. The performance between the proposed and existing

SRM drives is compared in detail. The major contributions and advantages of the proposed SRM drive can be summarized as follows.

1) By using the proposed SRM drive, the torque ripple and the vibration can be significantly reduced at both low and high speeds.
2) Compared to existing schemes, the torque output capacity of the SRM drive will not decrease with the reduction of the torque ripple and vibration.
3) The motor magnetic characteristics and online look-up-table are not previously required in the proposed drive and the computational complexity can be reduced.
4) The flexibility of the controller can be improved with the introduction of the *0*-axis current, which improves the robustness and fault-tolerant ability of the SRM drive.
5) The proposed scheme can be achieved by applying the modular six-switch converter, which shows a great potential for industrial application due to the modular topology.

REFERENCES

[1] E. Bostanci, M. Moallem, A. Parsapour, and B. Fahimi, "Opportunities and challenges of switched reluctance motor drives for electric propulsion: A comparative study," *IEEE Trans. Transp. Electrific.*, vol. 3, no. 1, pp. 58–75, Mar. 2017.

[2] C. Gan, J. Wu, Q. Sun, W. Kong, H. Li, and Y. Hu, "A review on machine topologies and control techniques for low-noise switched reluctance motors in electric vehicle applications," *IEEE Access*, vol. 6, pp. 31430–31443, 2018.

[3] J. Cai and Z. Deng, "Unbalanced phase inductance adaptable rotor position sensorless scheme for switched reluctance motor," *IEEE Trans. Power Electron.*, vol. 33, no. 5, pp. 4285–4292, May 2018.

[4] A. Chiba, K. Kiyota, N. Hoshi, M. Takemoto, and S. Ogasawara, "Development of a rare-earth-free SR motor with high torque density for hybrid vehicles," *IEEE Trans. Energy Convers.*, vol. 30, no. 1, pp. 175–182, Mar. 2015.

[5] M. Kawa, K. Kiyota, J. Furqani, and A. Chiba, "Acoustic noise reduction of a high-efficiency switched reluctance motor for hybrid electric vehicles with novel current waveform," *IEEE Trans. Ind. Appl.*, vol. 55, no. 3, pp. 2519–2528, May/Jun. 2019.

[6] C. Gan, N. Jin, Q. Sun, W. Kong, Y. Hu, and L. M. Tolbert, "Multiport bidirectional SRM drives for solar-assisted hybrid electric bus powertrain with flexible driving and self-charging functions," *IEEE Trans. Power Electron.*, vol. 33, no. 10, pp. 8231–8245, Oct. 2018.

[7] Y. Hu, C. Gan, Q. Sun, P. Li, J. Wu, and H. Wen, "Modular triport high-power converter for SRM based plug-in hybrid electrical trucks," *IEEE Trans. Power Electron.*, vol. 33, no. 4, pp. 3247–3257, Apr. 2018.

[8] Q. Sun, J. Wu, C. Gan, J. Si, J. Guo, and Y. Hu, "Cascaded multiport converter for SRM-based hybrid electrical vehicle applications," *IEEE Trans. Power Electron.*, vol. 34, no. 12, pp. 11940–11951, Dec. 2019.

[9] C. Gan, Q. Sun, J. Wu, W. Kong, C. Shi, and Y. Hu, "MMC-based SRM drives with decentralized battery energy storage system for hybrid electric vehicles," *IEEE Trans. Power Electron.*, vol. 34, no. 3, pp. 2608–2621, Mar. 2019.

[10] D. Panda and V. Ramanarayanan, "Reduced acoustic noise variable DC-bus-voltage-based sensorless switched reluctance motor drive for HVAC applications," *IEEE Trans. Ind. Electron.*, vol. 54, no. 4, pp. 2065–2078, Aug. 2007.

[11] H. Chang and C. Liaw, "Development of a compact switched-reluctance motor drive for EV propulsion with voltage-boosting and PFC charging capabilities," *IEEE Trans. Veh. Technol.*, vol. 58, no. 7, pp. 3198–3215, Sep. 2009.

[12] D. Wang, X. Du, D. Zhang, and X. Wang, "Design, optimization, and prototyping of segmental-type linear switched-reluctance motor with a toroidally wound mover for vertical propulsion application," *IEEE Trans. Ind. Electron.*, vol. 65, no. 2, pp. 1865–1874, Feb. 2018.

[13] V. Valdivia, R. Todd, F. J. Bryan, A. Barrado, A. Lazaro, and A. J. Forsyth, "Behavioral modeling of a switched reluctance generator for aircraft power systems," *IEEE Trans. Ind. Electron.*, vol. 61, no. 6, pp. 2690–2699, Jun. 2014.

[14] J. Borg Bartolo, M. Degano, J. Espina, and C. Gerada, "Design and initial testing of a high-speed 45-kW switched reluctance drive for aerospace application," *IEEE Trans. Ind. Electron.*, vol. 64, no. 2, pp. 988–997, Feb. 2017.

[15] S. Ullah, S. P. McDonald, R. Martin, M. Benarous, and G. J. Atkinson, "A permanent magnet assist, segmented rotor, switched reluctance drive for fault tolerant aerospace applications," *IEEE Trans. Ind. Appl.*, vol. 55, no. 1, pp. 298–305, Jan./Feb. 2019.

[16] F. Blaabjerg, P. C. Kjaer, P. O. Rasmussen, and C. Cossar, "Improved digital current control methods in switched reluctance motor drives," *IEEE Trans. Power Electron.*, vol. 14, no. 3, pp. 563–572, May 1999.

[17] K. M. Rahman, S. Gopalakrishnan, B. Fahimi, A. V. Rajarathnam, and M. Ehsani, "Optimized torque control of switched reluctance motor at all operational regimes using neural network," *IEEE Trans. Ind. Appl.*, vol. 37, no. 3, pp. 904–913, May/Jun. 2001.

[18] N. Yan, X. Cao, and Z. Deng, "Direct torque control for switched reluctance motor to obtain high torque–ampere ratio," *IEEE Trans. Ind. Electron.*, vol. 66, no. 7, pp. 5144–5152, Jul. 2019.

[19] N. K. Sheth and K. R. Rajagopal, "Optimum pole arcs for a switched reluctance motor for higher torque with reduced ripple," *IEEE Trans. Magn.*, vol. 39, no. 5, pp. 3214–3216, Sep. 2003.

[20] J. W. Lee, H. S. Kim, B. I. Kwon, and B. T. Kim, "New rotor shape design for minimum torque ripple of SRM using FEM," *IEEE Trans. Magn.*, vol. 40, no. 2, pp. 754–757, Mar. 2004.

[21] N. K. Sheth and K. R. Rajagopal, "Torque profiles of a switched reluctance motor having special pole face shapes and asymmetric stator poles," *IEEE Trans. Magn.*, vol. 40, no. 4, pp. 2035–2037, Jul. 2004.

[22] Y. K. Choi, H. S. Yoon, and C. S. Koh, "Pole-shape optimization of a switched-reluctance motor for torque ripple reduction," *IEEE Trans. Magn.*, vol. 43, no. 4, pp. 1797–1800, Apr. 2007.

[23] D. H. Lee, T. H. Pham, and J. W. Ahn, "Design and operation characteristics of four-two pole high-speed SRM for torque ripple reduction," *IEEE Trans. Ind. Electron.*, vol. 60, no. 9, pp. 3637–3643, Sep. 2013.

[24] P. O. Rasmussen, J. H. Andreasen, and J. M. Pijanowski, "Structural stator spacers-a solution for noise reduction of switched reluctance motors," *IEEE Trans. Ind. Appl.*, vol. 40, no. 2, pp. 574–581, Mar./Apr. 2004.

[25] C. Gan, J. Wu, M. Shen, S. Yang, Y. Hu, and W. Cao, "Investigation of skewing effects on the vibration reduction of three-phase switched reluctance motors," *IEEE Trans. Magn.*, vol. 51, no. 9, Sep. 2015, Art. no. 8203509.

[26] Z. Q. Zhu, X. Liu, and Z. Pan, "Analytical model for predicting maximum reduction levels of vibration and noise in switched reluctance machine by active vibration cancellation," *IEEE Trans. Energy Convers.*, vol. 26, no. 1, pp. 36–45, Mar. 2011.

[27] J. W. Ahn, S. J. Park, and D. H. Lee, "Hybrid excitation of SRM for reduction of vibration and acoustic noise," *IEEE Trans. Ind. Electron.*, vol. 51, no. 2, pp. 374–380, Apr. 2004.

[28] F. Lin and S. Yang, "Instantaneous shaft radial force control with sinusoidal excitations for switched reluctance motors," *IEEE Trans. Energy Convers.*, vol. 22, no. 3, pp. 629–636, Sep. 2007.

[29] A. D. Cheok and Y. Fukuda, "A new torque and flux control method for switched reluctance motor drives," *IEEE Trans. Power Electron.*, vol. 17, no. 4, pp. 543–557, Jul. 2002.

[30] H. J. Guo, "Considerations of direct torque control for switched reluctance motors," in *Proc. IEEE Int. Symp. Ind. Electron.*, Montreal, QC, Canada, Jul. 2006, pp. 2321–2325.

[31] A. Xu, C. Shang, J. Chen, J. Zhu, and L. Han, "A new control method based on DTC and MPC to reduce torque ripple in SRM," *IEEE Access*, vol. 7, pp. 68584–68593, Jun. 2019.

[32] R. B. Inderka and R. W. A. A. De Doncker, "DITC-direct instantaneous torque control of switched reluctance drives," *IEEE Trans. Ind. Appl.*, vol. 39, no. 4, pp. 1046–1051, Jul./Aug. 2003.

[33] J. Liang, D. H. Lee, and J. W. Ahn, "Direct instantaneous torque control of switched reluctance machines using 4-level converters," *IET Elect. Power Appl.*, vol. 3, no. 4, pp. 313–323, Jul. 2009.

[34] J. Ye, B. Bilgin, and A. Emadi, "An offline torque sharing function for torque ripple reduction in switched reluctance motor drives," *IEEE Trans. Energy Convers.*, vol. 30, no. 2, pp. 726–735, Jun. 2015.

[35] Q. Sun, J. Wu, C. Gan, Y. Hu, and J. Si, "OCTSF for torque ripple minimization in SRMs," *IET Power Electron.*, vol. 9, no. 14, pp. 2741–2750, Aug. 2016.

[36] S. Yao and W. Zhang, "A simple strategy for parameters identification of SRM direct instantaneous torque control," *IEEE Trans. Power Electron.*, vol. 33, no. 4, pp. 3622–3630, Apr. 2018.
[37] X. Liu *et al.*, "Performance comparison between unipolar and bipolar excitations in switched reluctance machine with sinusoidal and rectangular waveforms," in *Proc. IEEE Energy Convers. Congr. Expo.*, Sep. 2011, pp. 1590–1595.
[38] X. Liu, Z. Q. Zhu, M. Hasegawa, A. Pride, and R. Deodhar, "Investigation of PWMs on vibration and noise in SRM with sinusoidal bipolar excitation," in *Proc. IEEE Int. Symp. Ind. Electron.*, May 2012, pp. 674–679.
[39] X. Liu, Z. Q. Zhu, and Z. P. Pan, "Analysis of electromagnetic torque in sinusoidal excited switched reluctance machines having DC bias in excitation," in *Proc. 19th Int. Conf. Elect Mach.*, Sep. 2012, pp. 2882–2888.
[40] Z. Azar and Z. Q. Zhu, "Performance analysis of synchronous reluctance machines having nonoverlapping concentrated winding and sinusoidal bipolar with DC bias excitation," *IEEE Trans. Ind. Appl.*, vol. 50, no. 5, pp. 3346–3356, Sep./Oct. 2014.
[41] L. Du, B. Gu, J. J. Lai, and E. Swint, "Control of pseudo-sinusoidal switched reluctance motor with zero torque ripple and reduced input current ripple," in *Proc. IEEE Energy Convers. Congr. Expo.*, Sep. 2013, pp. 3770–3775.
[42] Q. Ma, X. Cui, L. Zhang, X. Zhao, and J. Lai, "Torque ripple and acoustic noise of current modulations of a pseudo-sinusoidal switched reluctance motor," in *Proc. IEEE Energy Convers. Congr. Expo.*, Sep. 2016, pp. 1–5.
[43] M. Cheng, H. Wen, P. Han, and X. Zhu, "Analysis of airgap field modulation principle of simple salient poles," *IEEE Trans. Ind. Electron.*, vol. 66, no. 4, pp. 2628–2638, Apr. 2019.
[44] D. Li, R. Qu, and J. Li, "Topologies and analysis of flux-modulation machines," in *Proc. IEEE Energy Convers. Congr. Expo.*, Sep. 2015, pp. 2153–2160.
[45] A. Toba and T. Lipo, "Generic torque-maximizing design methodology of surface permanent-magnet Vernier machine," *IEEE Trans. Ind. Appl.*, vol. 36, no. 6, pp. 1539–1546, Nov./Dec. 2000.
[46] D. Li, R. Qu, J. Li, L. Xiao, L. Wu, and W. Xu, "Analysis of torque capability and quality in vernier permanent-magnet machines," *IEEE Trans. Ind. Appl.*, vol. 52, no. 1, pp. 125–135, Jan./Feb. 2016.
[47] S. Jia, R. Qu, W. Kong, D. Li, and J. Li, "Flux modulation principles of DC-biased sinusoidal current vernier reluctance machines," *IEEE Trans. Ind. Appl.*, vol. 54, no. 4, pp. 3187–3196, Jul./Aug. 2018.
[48] B. Heller and V. Hamata, *Harmonic Field Effects in Induction Machines*. Amsterdam, The Netherlands: Elsevier, 1977.
[49] Z. Q. Zhu and D. Howe, "Instantaneous magnetic-field distribution in brushless permanent-magnet dc motors, part III: Effect of stator slotting," *IEEE Trans. Magn.*, vol. 29, no. 1, pp. 143–151, Jan. 1993.
[50] N. Bianchi and M. D. Pre, "Use of the star of slots in designing fractional slot single-layer synchronous motors," *Inst. Elect. Eng. Proc., Elect. Power Appl.*, vol. 153, no. 3, pp. 459–466, May 2006.
[51] Z. Q. Zhu, B. Lee, and X. Liu, "Integrated field and armature current control strategy for variable flux reluctance machine using open winding," *IEEE Trans. Ind. Appl.*, vol. 52, no. 2, pp. 1519–1529, Mar./Apr. 2016.
[52] J. Keyan and Z. Zhuo, "Study on direct torque control system of switched reluctance motor," in *Proc. 6th Int. Conf. Comput. Sci. Educ.*, Aug. 2011, pp. 904–908.
[53] A. Xu, W. Zhang, and P. Ren, "Comparison of torque ripple reduction for switched reluctance motor based on DTC and DITC," in *Proc. 13th IEEE Conf. Ind. Electron. Appl.*, 2018, pp. 1727–1732.
[54] S. Sau, R. Vandana, and B. G. Fernandes, "A new direct torque control method for switched reluctance motor with high torque/ampere," in *Proc. 39th Annu. Conf. IEEE Ind. Electron. Soc.*, Nov. 2013, pp. 2518–2523.

Zhiyue Yu (Student Member, IEEE) was born in Shandong, China, in 1996. He received the B.S. degree in electrical engineering and automation from Chongqing University, Chongqing, China, in 2018. He is currently working towards the M.S. degree with the School of Electrical and Electronic Engineering, Huazhong University of Science and Technology, Wuhan, China.

His research interests include the driving topology and control strategy of permanent magnet machines and reluctance machines.

Chun Gan (Member, IEEE) received the B.S. and M.S. degrees in electrical engineering from China University of Mining and Technology, Jiangsu, China, in 2009 and 2012, respectively, and the Ph.D. degree in electrical engineering and motor drives from Zhejiang University, Hangzhou, China, in 2016.

He is currently a Professor with the School of Electrical and Electronic Engineering, Huazhong University of Science and Technology, Wuhan, China. From 2016 to 2018, he was a Research Associate with the Department of Electrical Engineering and Computer Science, University of Tennessee, Knoxville, TN, USA. He has authored/coauthored more than 80 peer-reviewed technical papers, including more than 50 IEEE Transaction papers. He has more than 20 issued/published invention patents. His research interests include electric motor drives, electric motor converters, motor design, electric vehicles, electrified transportation, and high-efficiency power converters.

Dr. Gan was the recipient of the 2018 Highlighted Paper Award from IEEE TPEL, the 2018 Marie Sklodowska-Curie Actions Seal of Excellence Award from European Commission, and the 2019 Best Paper Award from ICEMS.

Yu Chen (Student Member, IEEE) was born in Changsha, China, in 1997. He received the B.S. degree in 2019 from the Huazhong University of Science and Technology, Wuhan, China, where he is currently working toward the Ph.D. degree with the School of Electrical and Electronic Engineering.

His research interests include high-efficiency power converters, advanced control strategies, and fault-tolerance schemes for electric motor systems.

Ronghai Qu (Fellow, IEEE) was born in China. He received the B.E.E. and M.S.E.E. degrees in electrical engineering from Tsinghua University, Beijing, China, in 1993 and 1996, respectively, and the Ph.D. degree in electrical engineering from the University of Wisconsin–Madison, Madison, WI, USA, in 2002.

In 1998, he joined the Wisconsin Electric Machines and Power Electronics Consortiums as a Research Assistant. He became a Senior Electrical Engineer with Northland, a Scott Fetzer Company, in 2002. Since 2003, he has been with the General Electric (GE) Global Research Center, Niskayuna, NY, USA, as a Senior Electrical Engineer with the Electrical Machines and Drives Laboratory. He has authored more than 50 published technical papers and holds more than 40 patents/patent applications. Since 2010, he has been a Professor with Huazhong University of Science &Technology, Wuhan, China.

Dr. Qu is a Full Member of Sigma Xi. He was the recipient of several awards from GE Global Research Center since 2003, including the Technical Achievement and Management Awards, the 2003 and 2005 Best Paper Awards, and Third Prize Awards from the Electric Machines Committee of the IEEE Industry Applications Society at the 2002 and 2004 IAS Annual Meeting.